PHYSICAL REVIEW B VOLUME 46, NUMBER 2 1 JULY 1992-II

Exciton-polariton luminescence from sodium cryptand sodide [Na^+(C222)Na^-]

Ta-Ryeong Park
Department of Physics and Astronomy and Center for Fundamental Materials Research, Michigan State University, East Lansing, Michigan 48824

Stuart A. Solin
NEC Research Institute, Princeton, New Jersey 08540

James L. Dye
Department of Chemistry and Center for Fundamental Materials Research, Michigan State University, East Lansing, Michigan 48824

(Received 31 May 1991; revised manuscript received 4 February 1992)

We have performed spatially and temporally resolved luminescence experiments on various-sized crystals of sodium cryptand [2.2.2] sodide to observe directly the spatial propagation of the optically excited state as well as the dependence of the luminescence specta on crystal size. Small crystals ($\leq \approx 50$ μm) exhibit a line shape that is distinct from that of larger crystals. A formalism based on polariton dynamics is developed to explain the time-evolution behavior and the dependence of the luminescence on crystal size.

I. INTRODUCTION

Sodium cryptand [2.2.2] sodide [Na^+(C222)Na^-], in which C222 represents the bicyclic polyether, cryptand[2.2.2],[1] is an ionic crystal in which both the positive and negative ions are derived from sodium metal.[2] This rather unusual sodium oxidation state of -1 is made possible by enclosure of the sodium positive ion in the cage structure of the multiatomic cryptand molecule, which serves to separate the positive and negative ions in the solid. The crystal structure[3] consists of close-packed cryptated cations with sodium anions in the pseudo-octahedral holes. The packing has an $A, B, C, A, \ldots$ sequence within a hexagonal unit cell in the space group $R32$ with $a = 8.83$ Å, and $C = 29.26$ Å. Sodium cryptand sodide, abbreviated Na^+(C222)Na^-, is one member of a class of compounds that contain alkali-metal anions. More than 40 such compounds, called alkalides have been synthesized and the crystal structures of 30 are known.[4] All alkalides are thermally unstable and reactive towards air and moisture, but can be handled and studied *in vacuo* or in an inert atmosphere below about $-40\,^\circ$C. Of all the alkalides the sodide used in this work, Na^+(C222)Na^- is the most stable and defect free and can be easily studied at low temperatures in an inert atmosphere. It can also be prepared as single crystals in the mm size range if desired.

Measurements of optical absorption have shown that films of Na^+(C222)Na^- have a broad absorption peak at 1.91 eV,[2] which can be identified with the same peak position found for Na^- in ethylenediamine. Therefore, the absorption peak in Na^+(C222)Na^- was attributed to the sodium anion's $3S \rightarrow 3P$ bound-bound transition, which could form an excitonic state. Recently, Bannwart *et al.* measured the photoluminescence spectrum of polycrystalline and single-crystal sodium cryptand[2.2.2] sodide by using an ultrafast picosecond pulsed dye laser as the excitation source.[5] The photoluminescence was attributed to a $3P \rightarrow 3S$ bound-bound transition of the sodium anion. The peak of the fluorescence occurred at about 1.84 eV with an excitation photon energy of 2.1 eV at a nominal temperature of 7 K.[6] Also, it was shown that the time evolution of this spectrum after ≈ 1 ns could be fit with a double exponential function. On the high-energy side of the band, two decay processes were observed, while on the low-energy side growth was followed by decay. The two time constants were independent of wavelength except on the high-energy edge, where they were both shorter. The results were interpreted as excitation from the narrow ground-state $3s$ band to a broad $3p$ band, followed by short-time emission from high-energy states in the p band. After decay to the bottom of the $3p$ band, excited-state relaxation was presumed to occur so that the long-time emission was from the relaxed excited state. At that time there was no evidence for mobility of the excited state, so a localized picture was used to explain the results. Because conductivity measurements had shown[7] that Na^+(C222)Na^- behaves as an intrinsic semiconductor with a band gap of ≈ 2.4 eV, the luminescence signal could not have arisen from the conduction band.

A puzzling feature of luminescence studies of sodides was the extremely weak signals from other sodides compared with that from Na^+(C222)Na^-.[8] The optical absorption spectra are similar, the ^{23}Na NMR signals are virtually identical, and the crystal structures clearly show that Na^- is present in all cases. The major difference between Na^+(C222)Na^- and other sodides is that the latter generally contain high concentrations (up to 1% or more) of defect electrons, whereas Na^+(C222)Na^- has barely detectable levels of trapped electrons. Both magnetic susceptibilities and EPR spectra confirm this difference.[9]

The weak luminescence from other sodides suggested that trapped electrons might be effective in quenching luminescence from sodides. If, however, the excitation remained localized, trapped electrons at low concentrations would not be effective quenchers. The experiments described in this paper were therefore performed to determine whether the excitation is localized or mobile.

Moreover the smallest separation between sodium anions is 8.83 Å, while the effective radius of the sodium metal anion is 2.5 Å. This implies that the ground-state wave function of the anion is well localized. However, despite the large separation, we expect sodium anions to interact through a dipole-dipole interaction (or higher order). Also the interstitial spaces and channels formed by packing of the large cations can provide room for the electron wave function to spread. This implies that there can be some overlap of the wave functions of neighboring sodium anions. The absorption spectrum of $Na^+(C222)Na^-$ films has a half width of 0.62 eV,[10] while that of the long-time (about 30 ns) luminescence spectrum is only 28 meV.[5] This also suggests that the wave function of the excited state of Na^- is broad enough to overlap with adjacent ions. Consequently, in spite of the very short lifetime of the excited state (a few nanoseconds) the possibility of excitation-energy transfer still remains. Thus, our experimental research focused on the search for mobile excited states that may exist in sodium cryptand[2.2.2] sodide.

In Sec. II we present a new set of experimental data based on the microluminescence method. In Sec. III we point out some of the deficiencies of the model presented in Ref. 5 and discuss the feasibility of the exciton-polariton picture as the process responsible for the photoluminescence signal. Finally in Secs. IV–VI we develop a mathematical model that is compared with previous and current experimental results in Sec. VII.

II. EXPERIMENTAL DETAILS AND RESULTS

In order to observe the propagation of the optically excited states directly, we employed a position-sensitive optical microscope whose objective was used both for focusing the laser light on the sample and for collecting the photoluminescence signal from the sample at a selected spot. Therefore in this microluminescence experiment, the signal was collected in the backward direction with a collection angle of about 15°. The size of the focused laser beam on the sample was about 10 μm. The light source consisted of a mode-locked Nd:YAG laser (Quantronix 416), which provided 1.06-mm, 100-ps-wide pulses at a 76-MHz repetition rate. Its output was frequency doubled to give about 1.2 W of 532-nm light that was used to pump a dye laser. The dye laser (Coherent model 702-CD) gave continuously tunable 6-ps-wide light pulses.

Since sodium cryptand[2.2.2] sodide does not give a stable luminescence signal at high laser light intensities (the intensity of the emission signal decreases gradually with time), we had to use low enough excitation light intensity in most cases to maintain the emission signal and sample stability. About 1 μW of time-averaged laser power was focused on the sample yielding a power density of about 1 W/cm^2. While performing experiments with a closed-cycle helium cryostat (Cryosystems LTS-21-.1), samples were kept in a vibration isolated chamber (connected to a Cryosystems SCA-Vib Vibration Isolation Adapter) that was connected to the cold finger of the cryostat with flexible copper wires (Fig. 1). The temperature sensor was attached to the sample chamber holder, and the monitored temperature was about 26 K. An *X-Y-Z* translator was used to bring the selected spot or sample into focus. The sample vibration amplitude and frequency were less than a few μm and a few hundred Hz, respectively. Moreover, considering the very fast optical and electronic processes, which are nearly completed in 30 ns, even slowly moving samples can be regarded as essentially stationary.

The signal was detected by a thermoelectrically cooled photomultiplier through a double grating monochromator. It was recorded on a multichannel analyzer using time-correlated photon counting methods[11] with a time-to-amplitude converter. Due to the low signal intensity, an inverted configuration of the time-to-amplitude converter was used. The overall instrument response time was about 0.7 ns. The dye laser pulse repetition rate was chosen to be 1 MHz and the excitation photon energy

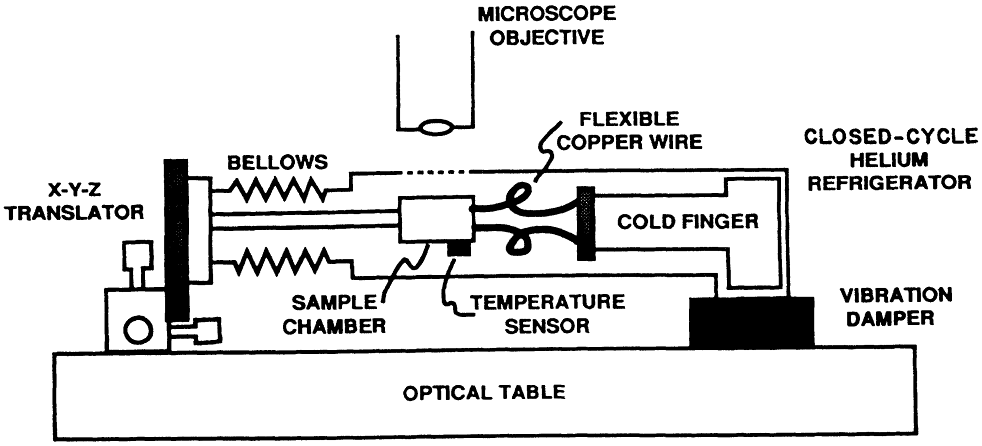

FIG. 1. Diagram of the low-temperature vibration isolated sample chamber with microscope.

was 2.1 eV.

Typical time and spatially resolved single-crystal data are shown in Fig. 2. Note the difference between the time-decay curves that were taken from two different spots on the same sample. The signal [designated by (*a*) in Fig. 2] emanating from a nonirradiated area (about 80 μm distant from illumination and 25 μm in diameter for signal collection) has a broader width in time and a peak position shifted toward later time than the one [designated by (*b*) in Fig. 2] from the illuminated area (25 μm in diameter for signal collection again). These time-resolved emission signals and the direct measurement of emission intensity as a function of distance from illumination (inset of Fig. 2) provide unambiguous proof that the optically excited state is propagating through the crystal. If the signal (*a*) were caused by direct laser light illumination (the very weak stray exciting laser light present at the position of signal collection), then its time dependence would be almost identical to the one represented by curve (*b*) considering the fact that one channel corresponds to 60 ps. In this experiment we scanned the exciting laser light across the sample surface with no change in the instrument response function within our experimental accuracy. Energy transport by a diffusion process can be considered to explain the slight peak position shift and the increase in decay width shown in Fig. 2. The exciton polariton, which is constantly scattered by acoustic phonons, while moving with the group velocity, is a viable medium for such energy transfer.

In the inset of Fig. 2 we have shown the time-integrated luminescence and exciting laser light intensities at various positions in order to give direct evidence that the emission from the nonilluminated position does not come from the stray exciting laser light but rather from the migration of the excited states. A rather broad distribution of the laser light, compared to the 10 μm beam size, is partially due to the wide signal collecting area (about 25 μm in diameter) and partially to the roughness of the sample surface that causes irregular reflection. Normally, the time decay [curve (*c*) in Fig. 2] at this energy (1.843 eV) from the large (order of 1 mm in size) and best quality (see below for the description of crystal quality) crystals is much slower than that shown by curves (*a*) and (*b*) in Fig. 2. The abnormally fast decay observed in Fig. 2 is attributed to lattice defects or impurities inside the crystal that enhance the nonradiative decay process. Sample quality is clearly discernible by the color it exhibits: this sample showed a less bright golden color than the one with the best quality. Therefore it should be noted that the emission intensity distribution appearing in the inset of Fig. 2 is only specific to the sample mentioned above.

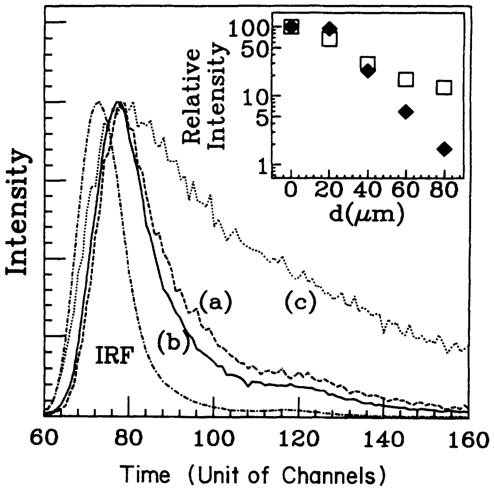

FIG. 2. Time-decay behavior of luminescence from (*a*) the nonilluminated spot and (*b*) the illuminated spot from sample 3 at an emission energy of 1.843 eV. IRF means instrumental response function. One channel = 60 ps. Inset: the spatial distribution of the laser excitation intensity (filled diamonds) and the emission signal intensity (empty squares) as a function of distance from the illumination spot with sample 3. Curve (*c*) is the time-decay curve at the same energy from a large ($\approx$1 mm in size) and shiny bright golden colored crystal.

Spectral line shapes have also been measured from various-sized crystals (1) shiny bright golden crystal $\approx$0.5 mm diameter (sample 1), (2) shiny bright golden powder $\approx$50 μm crystallite diameter (sample 2), and (3) less bright golden crystal $\approx$1 mm diameter (sample 3). Sample 3 was also used in obtaining the signal shown in Fig. 2. Figure 3(a) shows time-integrated line shapes. The time-integrated line shapes from powders ($\leq$50 μm in size) show a peak at 1.852 eV, which differs from the case of the larger samples. The spectrum of sample 3 has a dip at 1.845 eV and a larger width of 38 meV, while sample 1 shows no dip and a peak at lower energy with a width of 28 meV. Figure 3(b) shows the theoretical plotting of the time-integrated line shapes that correspond to the three experimental cases in Fig. 3(a). We will discuss this figure later.

Figure 4(a) shows the normalized time-resolved spectral line shapes of sample 3. We can see from Fig. 4(a) that the time-integrated line shape is largely composed of two components: (1) a narrow component with a relatively narrow width that decays rapidly with a peak at 1.852 eV and (2) a wide component that grows with time relative to the narrow one. A careful examination of Fig. 4(a) also shows that the narrow component has a peak position that is nearly unchanged, but the wide one changes continuously with time from a short wavelength to a long wavelength with time [Fig. 4(b)].

The time denoting our experimental line shapes is accurate only within our experimental time-resolution limit, 0.7 ns, determined by the instrumental response time. Therefore this limited time resolution does not give us true line shapes but only an average. This inaccuracy will be particularly large in the very-short-time region, less than $\approx$1 ns. Nevertheless, these curves are sufficient to provide us with a very clear trend.

From the above observations we conclude that the time-integrated photoluminescence line shapes are mainly determined by the crystal size and quality. A larger crystal yields a line shape with a peak at lower energy. A good-quality large crystal also has a much longer lifetime than either small crystals or large crystals with defects.

The normalized time-integrated line shapes from illuminated and nonilluminated spots (sample 3) are nearly identical except that the one from the illuminated area is slightly broader than the other. Neglecting this small difference, we will later use this observation as the experimental justification for the uniform distribution of polaritons, which we assume for simplicity.

III. MOTIVATION FOR THE EXCITON-POLARITON PICTURE

The three-level mechanism proposed in Ref. 5 is incomplete in accounting for various experimental observations. The proposed lower-energy level of the excited state, which is generated by relaxation of the surroundings would be determined by local interactions rather than long-distance effects. Hence, it can be said that the nature of the proposed induced energy level would be independent of the macroscopic geometry of the crystal. Therefore, this model does not provide a natural explanation for our crystal-size-dependent line shape. The interpretation of our data in terms of a mobile exciton-polariton[12–17] has many advantages. The spatial migration of the optical excitation can be understood as a result of diffusion of polaritons that are scattered by phonons. As was pointed out previously, the behavior shown in Fig. 2 is at least qualitative evidence for this diffusion. In order for the polaritons to luminesce, they first must gain access to the crystal boundary, where they are converted into photons. Consequently, the spectrum and time evolution (for example, lifetimes) of the polariton are affected by the crystal geometry, which controls the radiative decay rate.

The crystal-size-dependent line shape, shown in Fig. 3, is a convincing signature of exciton-polariton luminescence. Also, the continuous red shift of the spectrum as a function of time (Figs. 4 and 8; see also Ref. 5) is in qualitative agreement with polariton dynamics as was con-

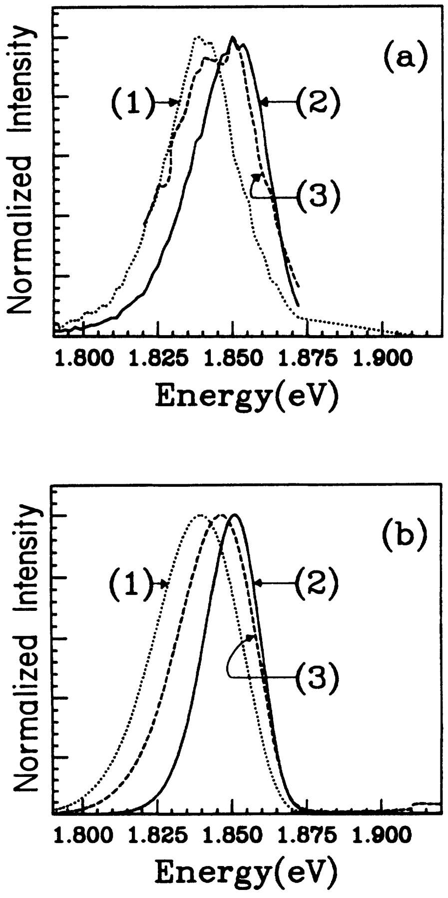

FIG. 3. (a) Experimental time-integrated luminescence line shapes from three crystals: (1) large (≈ 0.5 mm in size) and shiny bright golden colored crystal (sample 1), (2) small (≈ 50 μm) and shiny bright golden colored powder (sample 2), and (3) large (≈ 1 mm in size) and less shiny bright golden colored crystal than sample 1 (sample 3). (b) Corresponding theoretical time-integrated line shapes: (1) $S_c/V_c=0.5$/cm and $R_{\alpha 0}=2\times 10^8$/s, (2) $S_c/V_c=50$/cm and $R_{\alpha 0}=2\times 10^8$/s, and (3) $S_c/V_c=0.5$/cm and $R_{\alpha 0}=2\times 10^9$/s.

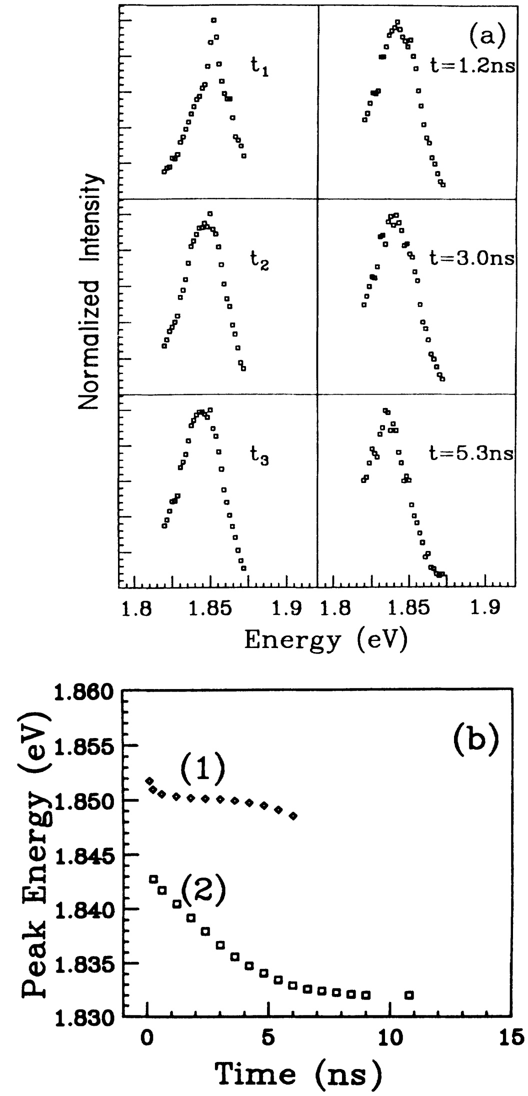

FIG. 4. (a) Time evolution of the luminescence line shapes from sample 3. $t_1 < t_2 < t_3 < \approx 1$ ns. (b) Peak energy vs time: (1) narrow and (2) wide component.

sidered by Toyozawa[15] who calculated the rate of energy decrease of a polariton as a result of scattering with phonons.

In addition to the above aspects, the time-decay characteristics of the photoluminescence signal from sodium cryptand[2,2,2] sodide are similar to those of CdS, CdSe,[17] and CdTe,[18] which are known to exhibit polariton luminescence. In general, these materials do not show single-exponential time-decay behavior (see Ref. 5 for the case of sodium cryptand[2,2,2] sodide, which was fitted with a double-exponential time decay). Also they show fast time decay at higher energy and slow decay at low energy, which means they have a time-dependent line shape.

Although many authors have addressed the theory of exciton-polariton luminescence,[16,17,19–22] none of their treatments was completely suitable for our purpose. In Ref. 16 steady-state luminescence from only the lower polariton branch was studied with a numerical method. In Ref. 19, the position-dependent but steady-state luminescence without radiative loss terms in the equations was considered. The treatments of Refs. 21 and 22 were also for steady-state luminescence only. In Ref. 17 the time-dependence of the luminescence was investigated, but numerical methods were used and crystal-size dependence was not considered.

IV. TRANSPORT EQUATIONS

It is well known that the strong coupling between photons and excitons[12,14] results in an additional excitation mode called an exciton-polariton whose dispersion relation, in the isotropic case,[23] is approximated by[14,17,24]

$$[n(\omega)]^2=\frac{c^2k^2}{\omega^2}=\epsilon_\infty+\frac{4\pi\beta\omega_0^2}{\omega_0^2+(\hbar\omega_0/m_e)k^2-\omega^2} \tag{1}$$

or

$$[n_{l,u}(\omega)]^2=\frac{c^2k_{l,u}^2}{\omega^2}=\frac{1}{2}\left[\epsilon_\infty-\left[1-\frac{\omega^2}{\omega_0^2}\right]\frac{m_ec^2\omega_0}{\hbar\omega^2}\right]\pm\left\{\frac{1}{4}\left[\epsilon_\infty+\left[1-\frac{\omega^2}{\omega_0^2}\right]\frac{m_ec^2\omega_0}{\hbar\omega^2}\right]^2+4\pi\beta\frac{m_ec^2\omega_0}{\hbar\omega^2}\right\}^{1/2}, \tag{2}$$

where the + sign refers to n_l, k_l, and the − sign refers to n_u, k_u in Eq. (2). In this equation, n_l and n_u are the indices of refraction of the lower polariton branch (LPB) and upper polariton branch (UPB), respectively, c is the speed of light in vacuum, $\mathbf{k}_{l,u}$ is the wave vector, ϵ_∞ is the background dielectric constant, m_e is the effective exciton mass, and β is the static polarizability of the exciton that satisfies[14,17]

$$(\Delta E)_{\mathrm{LT}}=E_{\mathrm{L}}(0)-E_{\mathrm{T}}(0)=\frac{2\pi\beta}{\epsilon_\infty}E_{\mathrm{T}}(0)\ . \tag{3}$$

Here, $E_{\mathrm{T}}(0)=\hbar\omega_0$ and $E_{\mathrm{L}}(0)$ are the transverse and longitudinal energy at $k=0$, respectively.

Following Askary and Yu,[17] we did not introduce a phenomenological damping constant in Eqs. (1) and (2) because we include radiative and nonradiative loss terms explicitly in our transport equations.

Since the observed luminescence spectrum depends on the polariton distribution function at the boundary of the crystal, it is necessary to set up transport equations appropriate to polariton dynamics. The transport equations are greatly simplified if we adopt a model that has an isotropic and spatially uniform polariton distribution. The latter can be partially justified with the experimental observation of the fact that the normalized spectral distributions at illuminated and unilluminated positions are nearly identical. The position dependent amplitude factor can be effectively compensated for by adjusting the geometry of the crystal appropriately. This will become clear in the discussion below.

Let $\bar{f}_\alpha(\mathbf{k},t)d^3r\,d^3k$ be the number of polaritons at branch α ($\alpha=l,u$) in the volume element $d^3r\,d^3k$ at time t, position $\mathbf{r}$, and wave vector $\mathbf{k}$. Then in the small $\bar{f}_\alpha(\mathbf{k},t)$ limit (weak excitation intensity limit) the transport equation for the LPB, after excitation by a laser pulse, is given by

$$\begin{aligned}\frac{\partial}{\partial t}\bar{f}_l(\mathbf{k},t)=&\frac{V_c}{(2\pi)^3}\int d^3k'[\overline{W}_{ll}(\mathbf{k}'\rightarrow\mathbf{k})f_l(\mathbf{k}',t)-\overline{W}_{ll}(\mathbf{k}\rightarrow\mathbf{k}')f_l(\mathbf{k},t)]\\&+\frac{V_c}{(2\pi)^3}\int d^3k'[\overline{W}_{ul}(\mathbf{k}'\rightarrow\mathbf{k})f_u(\mathbf{k}',t)-\overline{W}_{lu}(\mathbf{k}\rightarrow\mathbf{k}')f_l(\mathbf{k},t)]\\&-\frac{S_c}{V_c}\bar{v}_{gl}(\mathbf{k})[\overline{\Sigma}_l(\mathbf{k})+\overline{\Gamma}_l(\mathbf{k})]\bar{f}_l(\mathbf{k},t)-\overline{R}_l(\mathbf{k})\bar{f}_l(\mathbf{k},t)+\frac{S_c}{V_c}\bar{v}_{gu}(\mathbf{k})\overline{\Gamma}_u(\mathbf{k})\frac{g_u(E)}{g_l(E)}\bar{f}_u(\mathbf{k}'')\end{aligned} \tag{4}$$

in which $E_l(\mathbf{k})=E_u(\mathbf{k}'')=E$, representing the same energy of the LPB and UPB that have different wave vectors. We obtain a similar equation for the UPB by exchanging the indices l with u in Eq. (4). Here $\bar{v}_{g\alpha}(\mathbf{k})$ is the group velocity of the polariton at branch α, V_c and S_c are the crystal volume and surface area, respectively, $\overline{R}_\alpha(\mathbf{k})$ is the nonradiative loss rate of the branch α, $\overline{W}_{\alpha\beta}(\mathbf{k}'\rightarrow\mathbf{k})$ is the transition rate due to scattering with phonons from polariton branch α with wave vector $\mathbf{k}'$ to β with $\mathbf{k}$, $g_\alpha(E)$ is the density of states at branch α, and $\overline{\Sigma}_\alpha$ and $\overline{\Gamma}_\alpha$

will be defined later. In Eq. (4) the first term on the right-hand side represents the intrabranch scattering in the LPB and the second term the interbranch scattering from and to the UPB. The term $(S_c/V_c)\overline{v}_{gl}(\mathbf{k})\Sigma_l(\mathbf{k})\overline{f}_l(\mathbf{k},t)$ represents the radiative loss due to the transmission of polaritons into the vacuum as photons,

$$(S_c/V_c)\overline{v}_{gl}(\mathbf{k})\Gamma_l(\mathbf{k})\overline{f}_l(\mathbf{k},t)$$

is the interbranch conversion loss from LPB to UPB and

$$(S_c/V_c)\overline{v}_{gu}(\mathbf{k})\Gamma_u(\mathbf{k})[g_u(E)/g_l(E)]\overline{f}_u(\mathbf{k}'',t)$$

is the interbranch conversion gain from UPB to LPB. (As in Ref. 17, we have neglected the longitudinal exciton band in these transport equations, for simplicity. However, it is not neglected in calculating the transmission coefficient etc., in Sec. VI.)

All those processes that involve transmission to vacuum and the interbranch conversion occur at the crystal-to-vacuum boundary. Therefore these terms are directly responsible for the crystal-size dependence of the spectra that we have observed experimentally.

Since the experimental observations are usually made in terms of energy (or wavelength), it is convenient to rewrite Eq. (4) and its companion equation for the UPB in terms of energy instead of wave vector. We construct equations regarding the number of polaritons per unit energy interval, $\phi_\alpha(E,t)$. Then with

$$\phi_\alpha(E,t)=V_c g_\alpha(E)\overline{f}_\alpha(k(E),t)\equiv V_c g_\alpha(E)f_\alpha(E,t) \tag{5}$$

and

$$\frac{V_c}{(2\pi)^3}\int d^3k'[\overline{W}_{\alpha\beta}(\mathbf{k}\to\mathbf{k}')\phi_\alpha(E(\mathbf{k}),t)] \equiv \int dE' Z_{\alpha\beta}(E\to E')\phi_\alpha(E,t)\ , \tag{6}$$

Eq. (4) becomes

$$\begin{aligned}\frac{\partial}{\partial t}\phi_l(E,t)=&\int dE'[\phi_l(E',t)Z_{ll}(E'\to E)-\phi_l(E,t)Z_{ll}(E\to E')]-\left[\frac{S_c}{V_c}v_{gl}(E)[\Sigma_l(E)+\Gamma_l(E)]+R_l(E)\right]\phi_l(E,t)\\&+\int dE'[\phi_u(E',t)Z_{ul}(E'\to E)-\phi_l(E,t)Z_{lu}(E\to E')]+\frac{S_c}{V_c}v_{gu}(E)\Gamma_u(E)\phi_u(E,t)\end{aligned} \tag{7}$$

and there is a corresponding equation for the UPB, where

$$v_{gl}(E(\mathbf{k}))\equiv\overline{v}_{gl}(\mathbf{k})\ , \tag{8}$$

etc. In the equation for the UPB we neglect the intrabranch scattering, since, because of the small density of states and the small magnitude of the wave vector of the UPB, it is much smaller than the interbranch scattering rate. [See the expression for $\overline{W}_{\alpha\beta}(\mathbf{k}'\to\mathbf{k})$ below and the intrabranch scattering term in Eq. (4).]

The expression for the polariton scattering rate with longitudinal acoustic phonons has been taken from Ref. 25 as follows (we consider only LA phonons as the dominant scattering source responsible for the polariton evolution, while scattering with optical phonons is assumed to occur just after the excitation by the laser pulse):

$$\overline{W}_{\alpha\beta}(\mathbf{k}'\to\mathbf{k})=\left[\frac{2\pi}{\hbar}\right]\left[\frac{\hbar D^2}{2\rho\mu V_c}\right]q\Lambda_{\alpha\beta}(\mathbf{k}'\to\mathbf{k})\{N_p(\hbar\mu q)\delta(E_f-E_i-\hbar\mu q)+[N_p(\hbar\mu q)+1]\delta(E_f-E_i+\hbar\mu q)\}\ , \tag{9}$$

where $q=|\mathbf{k}'-\mathbf{k}|$, μ is the speed of sound, D the exciton deformation potential, ρ the density of the crystal, $N_p(\hbar\mu q)$ the number of the phonons per state with energy $\hbar\mu q$ at a given temperature, E_i (E_f) the initial (final) -state polariton energy and $\Lambda_{\alpha\beta}(\mathbf{k}'\to\mathbf{k})$ is given by

$$\Lambda_{\alpha\beta}(\mathbf{k}'\to\mathbf{k})=|u_\beta^*(\mathbf{k})u_\beta(\mathbf{k}')+v_\beta(\mathbf{k})v_\alpha^*(\mathbf{k}')|^2=\Lambda_{\beta\alpha}(\mathbf{k}\to\mathbf{k}') \tag{10}$$

with

$$u_\alpha(\mathbf{k})=i\left[\frac{\pi\beta}{\epsilon_\infty\omega_\alpha(k)\omega_k L_{\alpha k}}\right]^{1/2}\left[\frac{\omega_\alpha(k)+\omega_k}{1-\omega_\alpha(k)^2/\omega_k^2}\right]\quad(\alpha=l,u)\ , \tag{11}$$

$$L_{\alpha k}=1+\frac{4\pi\beta/\epsilon_\infty}{[1-\omega_\alpha^2(k)/\omega_k^2]^2}\ , \tag{12}$$

$$v_\alpha(-\mathbf{k})=-\left[\frac{\omega_k-\omega_\alpha(k)}{\omega_k+\omega_\alpha(k)}\right]u_\alpha(\mathbf{k})\ , \tag{13}$$

where

$$\hbar\omega_k=\hbar\omega_0+\frac{\hbar^2k^2}{2m_e} \tag{14}$$

and $\hbar\omega_\alpha(k)$ is the polariton energy of the branch α with wave vector k.

In evaluating the interbranch scattering terms due to LA phonons in Eq. (7), we have adopted some simplifying approximations from Ref. 25. Owing to the small magnitude of the LA phonon wave vector in the region of interest, the inter-branch scattering was regarded as elastic, and, in considering the intrabranch scattering, we have neglected the change in magnitude of the LPB polariton wave vector after being scattered by a phonon. (See Section III A of Ref. 25 for details.) Then we have

$$\int dE'\phi_u(E',t)Z_{ul}(E'\to E)=\Delta(E)g_l(E)k_l(E)\phi_u(E,t)\Theta(E-E_L)\ , \tag{15}$$

$$\int dE'\phi_l(E,t)Z_{lu}(E\to E')=\Delta(E)g_u(E)k_l(E)\phi_l(E,t)\Theta(E-E_L)\ , \tag{16}$$

and the corresponding equations for the UPB. Here

$$\Delta(E)=\frac{\pi D^2}{\rho\mu}[2N_p(\hbar\mu k_l(E))+1]\Lambda_{ul}(k_u(E)\to k_l(E))\ , \tag{17}$$

and $k_\alpha(E)$ is the wave vector of the polariton branch α whose energy is E.

The intrabranch (LPB) scattering term due to LA phonons in Eq. (7) plays a very important role in determining the time evolution of the polariton luminescence. By its appearance only, we see that the LPB polaritons are undergoing a diffusion process in energy space. (If we relax the condition of a spatially uniform distribution, polaritons will also diffuse over space.) We can simplify the intrabranch scattering term in a manner analogous to the procedure used for deriving the Fokker-Planck equation.[26] For this purpose we define, for $\varepsilon>0$,

$$Z_{ll}(E\to E+\varepsilon)\equiv Z_+(E;\varepsilon) \tag{18}$$

and

$$Z_{ll}(E\to E-\varepsilon)\equiv Z_-(E;-\varepsilon)\ . \tag{19}$$

Then, since in our approximation (see Ref. 25),

$$q=|\mathbf{k}'-\mathbf{k}|\simeq 2k\sin(\phi/2)\ , \tag{20}$$

where ϕ is the angle between $\mathbf{k}'$ and $\mathbf{k}$, we have

$$0\le\varepsilon\le 2k\hbar\mu\equiv\varepsilon_m\ . \tag{21}$$

Therefore the first term on the right-hand side of Eq. (7) is approximated by

$$\begin{aligned}\int dE'[\phi_l(E',t)Z_{ll}(E'\to E)-\phi_l(E,t)Z_{ll}(E\to E')]\simeq{}&\frac{\partial}{\partial E}\left[\phi_l(E,t)\int_0^{\varepsilon_m}dS\,S[Z_-(E;-S)-Z_+(E;S)]\right]\\&+\frac{1}{2}\frac{\partial^2}{\partial E^2}\left[\phi_l(E,t)\int_0^{\varepsilon_m}dS\,S^2[Z_-(E;-S)+Z_+(E;S)]\right]\end{aligned} \tag{22}$$

and for $E'\ge E$

$$\begin{aligned}\int_{E'\ge E}dE'Z_{ll}(E\to E')&=\int d\epsilon Z_+(E;\epsilon)\\&\simeq\frac{1}{(2\pi)^3}\int dk_l'(E)4\pi k_l'^2(E)\frac{d\Omega}{4\pi}\frac{\pi D^2}{\rho\mu}\Lambda_{ll}(\mathbf{k}_l(E)\to\mathbf{k}_l'(E))N_p(\hbar\mu q)\delta(E_f-E_i-\hbar\mu q)\\&=g_l(E)\frac{\pi D^2}{\rho\mu}\Lambda_{ll}(\mathbf{k}_l(E)\to\mathbf{k}_l'(E))\frac{1}{2k_l^2(E)(\hbar\mu)^3}\int_{\varepsilon=0}^{\varepsilon=2k\hbar\mu}\varepsilon^2N_p(\varepsilon)d\varepsilon\ ,\end{aligned} \tag{23}$$

where

$$d^3k_l'(E)=k_l'^2(E)dk_l'(E)d\Omega\ . \tag{24}$$

Thus we obtain

$$Z_+(E;\varepsilon)=\frac{\pi D^2}{\rho\mu}\Lambda_{ll}(\mathbf{k}_l(E)\to\mathbf{k}_l(E))\frac{g_l(E)N_p(\varepsilon)\varepsilon^2}{2k_l^2(E)(\hbar\mu)^3} \tag{25}$$

and a corresponding expression for $Z_-(E;-\varepsilon)$ with $N_p(\varepsilon)\to[N_p(\varepsilon)+1]$.

Combining Eqs. (7), (15)–(17), (22), and (25), we obtain the following balance equations for the lower and upper polaritons:

$$\frac{\partial}{\partial t}\phi_l(E,t)\simeq\frac{\partial}{\partial E}[A(E)\phi_l(E,t)]+\frac{1}{2}\frac{\partial^2}{\partial E^2}[H(E)\phi_l(E,t)]-B(E)\phi_l(E,t)+C(E)\phi_u(E,t)\ , \tag{26}$$

$$\frac{\partial}{\partial t}\phi_u(E,t)\simeq-\beta(E)\phi_u(E,t)+\alpha(E)\phi_l(E,t)\ , \tag{27}$$

where

$$\alpha(E)=\left[\frac{S_c}{V_c}v_{gl}(E)\Gamma_l(E)+\Delta(E)g_u(E)k_l(E)\right]\Theta(E-E_L)\ , \tag{28}$$

$$\beta(E)=\left[\frac{S_c}{V_c}v_{gu}(E)[\Sigma_u(E)+\Gamma_u(E)]+R_u(E)+\Delta(E)g_l(E)k_l(E)\right]\Theta(E-E_L)\ , \tag{29}$$

$$A(E)=\frac{D^2}{\pi\rho}\frac{k_l^4}{v_{gl}(E)}\Lambda_{ll}(k_{ll}(E)\rightarrow k_l(E))\ , \tag{30}$$

$$B(E)=\frac{S_c}{V_c}v_{gl}(E)[\Sigma_l(E)+\Gamma_l(E)]+R_l(E)+\Delta(E)g_u(E)k_l(E)\Theta(E-E_L)\ , \tag{31}$$

$$C(E)=\left[\frac{S_c}{V_c}v_{gu}(E)\Gamma_u(E)+\Delta(E)g_l(E)k_l(E)\right]\Theta(E-E_L)\ , \tag{32}$$

and

$$H(E)=\frac{\pi D^2}{\rho\mu}\Lambda_{ll}(k_l(E)\rightarrow k_l(E))\frac{g_l(E)}{2k_l^2(E)(\hbar\mu)^3}\int_0^{2\hbar\mu k_l(E)}[2N_p(S)+1]S^4dS\ . \tag{33}$$

As for the nonradiative decay rate $R_\alpha(E)$ due to either lattice defects or impurities, we have taken Sumi's expression,[16] which is given by

$$R_\alpha(E)=R_{\alpha0}|u_\alpha(E)|^2\ , \tag{34}$$

where $R_{\alpha0}$ is a constant.

V. APPROXIMATE SOLUTIONS

Since the photons incident on the crystal are converted into excitons at $t=0$, the initial conditions will be

$$\phi_u(E,0)=0 \ \text{ and } \ \phi_l(E,0)\neq 0\ . \tag{35}$$

Therefore

$$\phi_u(E,t)=\alpha(E)e^{-\beta(E)t}\int_0^t e^{\beta(E)t'}\phi_l(E,t')dt'\ . \tag{36}$$

Equation (26) for the LPB population in its present form is difficult to solve. The terms $-B\phi_l$ and $C\phi_u$ contribute to the loss and gain, respectively. Without those loss and gain terms, Eq. (26) becomes a Fokker-Planck equation that describes the diffusion of LPB polaritons in energy space. And our earlier choice of $\phi_l(E,t)$ is compatible with this picture in the respect that the integration of $\phi_l(E,t)$ over the entire energy space gives a time-independent constant in the absence of loss and gain terms, as is readily checked with Eq. (4). Consequently, the two terms including $A(E)$ and $H(E)$ are crucial in determining the time evolution of the observed line shape. (Of course the line shape is determined not only by population but also by other factors such as the transmission coefficient.)

Therefore we separate the steep energy-dependent part determined by the Fokker-Planck equation from the overall time-evolution part, which is dominated by gain and loss terms. We write

$$\phi_l(E,t)\simeq\Omega(E,t)G(E,t),\ \frac{\partial\Omega}{\partial E}\simeq 0\ , \tag{37}$$

and the equation for $G(E,t)$ is chosen to be

$$\frac{\partial}{\partial t}G(E,t)\simeq\frac{\partial}{\partial E}[A(E)G(E,t)]+\frac{1}{2}\frac{\partial^2}{\partial E^2}[H(E)G(E,t)]\ . \tag{38}$$

Then we obtain

$$\phi_l(E,t)\simeq G(E,t)e^{-Bt}\left[1+C\int_0^t e^{Bt'}\frac{\phi_u(E,t')}{G(E,t')}dt'\right]\ . \tag{39}$$

Therefore, in this approximation our problem reduces to solving the Fokker-Planck equation given by Eq. (38) and solving Eq. (36) and (39) simultaneously. As a further approximation for solving Eq. (38), we can replace $A(E)$ and $H(E)$ with $A(E_m)$ and $H(E_m)$, where E_m is the energy at which the maximum of $G(E,t)$ occurs at time t. This is a reasonable approximation because the full width at half maximum (FWHM) of the experimental line shape is about 28 meV, while the energy range in which polaritons evolve is about 310 meV (from 2.1 to 1.79 eV). [The FWHM of the function $G(E,t=30\text{ ns})$ is about 50 meV (Fig. 5) by this approximation with the parameters in Table I.] Consequently $A(E)$ and $H(E)$ are treated as if they were functions of time, since $E_m=E_m(t)$. Hence, Eq. (38) is rewritten as

$$\frac{\partial}{\partial t}G(E,t)\simeq A(E_m(t))\frac{\partial}{\partial E}G(E,t)+\tfrac{1}{2}H(E_m(t))\frac{\partial^2}{\partial E^2}G(E,t)\ . \tag{40}$$

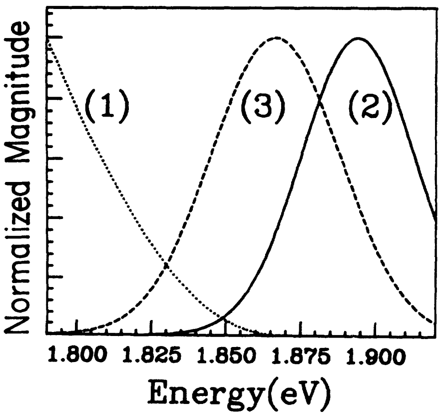

FIG. 5. Energy dependence of (1) multiplicative factor $T_l v_{gl}/n_l^2$, (2) $G(E,\ t=1$ ns), and (3) $G(E,\ t=30$ ns).

In order to solve Eq. (40) we define $\xi(t)$ and $\nu(t)$ as follows:

$$-\int_{E_0}^{\xi(t)} \frac{dE}{A(E)} = t \ , \tag{41}$$

$$-\int_{E_0}^{\xi(t)} \frac{H(E)}{A(E)} d(E) = \nu(\xi(t)) = \nu(t) \ , \tag{42}$$

where $\xi = \xi(E_0, t) = \xi(t)$ and E_0 is the appropriate initial onset energy (taken as a parameter) at which the diffusion of polaritons by the scattering with LA phonons begins. (This initial onset energy can be lower than the laser excitation energy since polaritons are scattered by optical phonons at very early times.) Then we see that

$$G(E,t) = \frac{1}{[\nu(t)]^{1/2}} \exp\left[-\frac{[E-\xi(t)]^2}{2\nu(t)} \right] \tag{43}$$

satisfies Eq. (40) with

$$E_m(t) = \xi(t) \ . \tag{44}$$

Thus we see that $E_m(t)$ is indeed the maximum energy corresponding to the peak of $G(E,t)$ at time t. With Eq. (41) it is evident that the maximum energy decreases monotonically as time increases and that the rate of change slows down, since the magnitude of $A(E)$ becomes smaller at smaller energies.

Equations (36) and (39) for $\phi_u(E,t)$ and $\phi_l(E,t)$ can be solved by iteration, for $E > E_L$. Since $G(E,t)$ approaches its long-time value rapidly, it can be approximated by its latest value when it appears in the integrand of Eqs. (36) and (39). Then we have

$$\phi_u^{(N)}(E,t) = \alpha e^{-\beta t} \int_0^t e^{\beta t'} \phi_l^{(N-1)}(E,t')dt' \quad (N \geq 1) \ , \tag{45}$$

$$\phi_l^{(N)}(E,t) = Ge^{-Bt} + Ce^{-Bt} \int_0^t e^{Bt'} \phi_u^{(N)}(E,t')dt' \quad (N \geq 1) \ , \tag{46}$$

where $\phi_\alpha^{(N)}(E,t)$, $\alpha = 1,u$, denotes the value of $\phi_\alpha(E,t)$ obtained after performing the Nth integration. Obviously, the LPB population $\phi_l(E,t)$ dominates over the UPB $\phi_u(E,t)$, since the probability for a transition from the LPB to the UPB is much smaller than the opposite transition due to the difference in density of final states. [Eqs. (15), (16), and the corresponding equations for the UPB]. Hence, we choose

$$\phi_l^{(0)}(E,t) = G(E,t)e^{-B(E)t} \ , \tag{47}$$

$$\phi_u^{(0)}(E,t) = 0 \ . \tag{48}$$

Successive iteration with the terms of small contribution neglected leads to a convergent result that is given by

$$\phi_l(E,t) \simeq G(E,t) \exp\left[-\left(B - \frac{\alpha C}{\beta - B} \right) t \right] \ , \tag{49}$$

$$\phi_u(E,t) \simeq G(E,t) \frac{\alpha}{\beta} \left\{ \exp\left[-\left(B - \frac{\alpha C}{\beta - B} \right) t \right] - e^{-\beta t} \right\} \ . \tag{50}$$

Equations (49) and (50) give self-consistent results when inserted into Eqs. (36) and (39), since $\beta \gg B$ and $\beta \gg \alpha C / \beta$.

TABLE I. The parameters used in the calculations (see text).

Background dielectric constant $(\epsilon_\infty) = 6$
Longitudinal to transverse splitting $(\beta) = 0.02$
Effective exciton mass $(m_e) = 0.12$ electron mass
Exciton deformation potential $(D) = 9$ eV
Density (ρ) (from Ref. 3) $= 1.064$ g/cm^3
Longitudinal exciton minimum energy $(E_L) = 1.91$ eV
Initial onset energy $(E_0) = 2.0$ eV
LA phonon sound speed $(\mu) = 3 \times 10^5$ cm/s
Temperature $(T) = 20$ K

Ratio of surface area to volume of crystal $(S_c/V_c) = 0.5$/cm
Nonradiative decay constants $(R_{\alpha 0},\ \alpha = 1,u) = 2 \times 10^8$/s

VI. RADIATIVE LOSS AND INTERBRANCH CONVERSION

The transmission coefficient as a function of energy and incident angle of the polariton directly determine the radiative loss, and this has been considered by many workers.[15-17] A larger transmission means a larger radiative loss. Therefore, it has a simple relationship with $\Sigma_\alpha(E)$:

$$\Sigma_\alpha(E) = \frac{1}{2} \int_0^{\theta_\alpha^{\mathrm{T}}} \cos\theta \sin\theta T_\alpha(E;\theta) d\theta \quad (\alpha = l,u) \ , \tag{51}$$

where $T_\alpha(E;\theta)$ is the transmission coefficient of the polariton branch α at energy E with an incident angle of θ. In the same way the interbranch conversion rate is given by

$$\Gamma_\alpha(E) = \frac{1}{2} \int_0^{\theta_\alpha^{\mathrm{IC}}} \cos\theta \sin\theta I_{\alpha\beta}(E;\theta) d\theta \quad (\alpha\beta = lu \text{ or } ul) \tag{52}$$

where $I_{\alpha\beta}(E;\theta)$ is the interbranch conversion coefficient from polariton branch α to β, $\alpha \neq \beta$, at energy E with incident angle θ. In Eqs. (51) and (52) the angles $\theta_\alpha^{\mathrm{T}}$ and $\theta_\alpha^{\mathrm{IC}}$ are determined by the relations

$$\sin\theta_\alpha^{\mathrm{T}} = \frac{1}{n_\alpha(E)} (\alpha = l,u) \tag{53}$$

and

$$\sin\theta_l^{\mathrm{IC}} = \frac{n_u(E)}{n_l(E)}, \quad \sin\theta_u^{\mathrm{IC}} = \frac{\pi}{2} \quad \text{for } E \geq E_L \ . \tag{54}$$

Here for an angle greater than θ_α^T, total reflection occurs. And for an angle greater than θ_l^{IC}, the wave vector of the polariton converted from the LPB to the UPB becomes complex with a pure imaginary component, which is normal to the surface. It is given by

$$(k_u^R)_Z = -ik_l^I(\sin^2\theta - \sin^2\theta_l^{\mathrm{IC}}) \tag{55}$$

(see Ref. 27 for a similar argument in the case of total reflection) where k_l^I is the magnitude of the incident LPB polariton. Therefore, for $\theta > \theta_l^{\mathrm{IC}}$ the converted UPB polaritons do not propagate, and there is no interbranch conversion from the LPB to the UPB.

Following Selkin,[28] the transmission coefficient has been obtained by taking the ratio of the magnitude of the time-averaged transmitted energy flux to the magnitude of the incident flux. (In our case we are considering the transmission from inside the crystal to vacuum.) The interbranch conversion coefficient has been similarly obtained. Using the expression for the time-averaged energy flux of Ref. 28 we find explicitly

$$T_\alpha(E;\theta) = \left| \frac{E_\alpha^T}{E_\alpha^I} \right|^2 \left| \frac{\mathrm{Re}(k_\alpha^T)}{\mathrm{Re}(k_\alpha^I)} \right| \frac{1}{1+\zeta\chi_\alpha^2} \tag{56}$$

and

$$I_{\alpha\beta}(E;\theta) = \left| \frac{E_\beta^R}{E_\alpha^I} \right|^2 \left| \frac{\mathrm{Re}(k_\beta^R)}{\mathrm{Re}(k_\alpha^I)} \right| \frac{1+\zeta\chi_\beta^2}{1+\zeta\chi_\alpha^2} \quad (\alpha,\beta = l,u \ \text{ and } \alpha \neq \beta) \tag{57}$$

where

$$\chi_\alpha = (n_\alpha^2 - \epsilon_\infty)/4\pi \ \text{ and } \zeta = \frac{4\pi\hbar\omega^2}{\beta m_e c^2 \omega_0} \ , \tag{58}$$

and E_α^I is the incident electric-field amplitude of the branch α with angle θ, E_α^T is the corresponding transmitted vacuum amplitude, E_β^R is the converted (reflected) amplitude inside the crystal, and the k's are the wave vectors that carry a similar meaning.

In evaluating the various ratios of the electric fields for Eqs. (57) and (58), we have used Pekar's ABC (additional boundary condition) (see Ref. 17 and the references therein for a discussion of the ABC). In the case of p polarization, we have included the contribution from the longitudinal exciton band also. Then we have used the average value over s and p polarizations for T_α and $I_{\alpha\beta}$.

VII. COMPARISON WITH EXPERIMENT

We begin our discussion with the expression of the line shape from polariton luminescence. When the luminescence signal is collected with a fixed small solid angle $\Delta\Omega_{\mathrm{ex}}$ at normal emergence of the luminescence, we have[19,25] as the relationship for the line shape $I(E,t)$

$$I(E,t)\Delta\Omega_{\mathrm{ex}}\Delta E = \sum_{\alpha=l,u} T_\alpha(E;0) v_{g\alpha}(E) g_\alpha(E) f_\alpha(E) \frac{\Delta\Omega_{\mathrm{ex}}}{n_\alpha^2(E)} \tag{59}$$

or

$$I(E,t) \propto \sum_{\alpha=l,u} \frac{T_\alpha(E;0) v_{g\alpha}(E)}{n_\alpha^2(E)} \phi_\alpha(E,t) \ . \tag{60}$$

Since $\beta(E) \gg \alpha(E)$ through the contribution of the density of states, the surface terms (radiative loss and interbranch conversion) and the nonradiative decay term [see Eqs. (28) and (29)] we have $\phi_l(E,t) \gg \phi_u(E,t)$. Therefore, the main contribution to the total luminescence arises from the LPB even with the multiplicative terms $T_\alpha(E;0)v_{g\alpha}(E)/n_\alpha^2(E)$. [However, it should be noted that without the surface terms and the nonradiative loss term in Eqs. (28) and (29), the UPB makes an equally important contribution to the total luminescence due to the modulating multiplicative factors.] Therefore, as was pointed out by Askary and Yu,[17] the UPB mainly manifests itself not through a sizable luminescence in comparison to the LPB but by affecting the transmission coefficient of the LPB through the additional boundary condition and affecting the overall decay rate of the LPB, which depends on the ABC through the surface terms. Since in the region of interest $\phi_l(E,t)$ and $G(E,t)$ are increasing functions of energy and $T_l(E;0)v_{gl}(E)/n_l^2(E)$ is a rapidly decreasing function of energy (see Fig. 5), their product shows a curve that has a well-defined peak that shifts in time according to the evolution of the function $G(E,t)$. It is worth emphasizing that the observed luminescence distribution is different from the polariton population distribution because of the extremely small overall escape probability of LPB polaritons due to their excitonic nature at higher energy.

Figure 6(a) shows a theoretical plot of the energy at maximum intensity as a function of time with the parameters given in Table I, and Fig. 6(b) shows the time evolution of the line shape from 1 to 30 ns. They show a very good agreement with the experimental observation, as shown in Fig. 6(c) and reported in Ref. 5. Figure 6(c) shows the corresponding experimental time-resolved line shapes from a large (≈ 1 mm in size) crystal. In choosing the parameters listed in Table I, the nonradiative decay loss constant, $R_{\alpha 0}$, defined in Eq. (34) had to be fixed at 2×10^8/s for a shiny bright golden colored (of best quality) and large (≈ 1 mm in size) crystal in order to match the long lifetime of about 5 ns measured in Ref. 5. This is required because the radiative decay loss rate of the LPB decreases severely near and above the longitudinal exciton band-minimum energy for reasonable combinations of parameters. (See below for the discussion of the lifetimes.) Therefore, it can be said that the long lifetimes of the shiny bright golden colored and large (≈ 1 mm in size) crystals of Ref. 5 are mainly determined by lattice defects and impurities, according to the parameter combination of Table I.

In order to make a direct comparison with experiment it is very helpful to examine the time evolution of the luminescence at fixed energies in addition to the information shown in Fig. 6.

Equation (60) for the total luminescence becomes approximately

$$
\begin{aligned}
I(E,t) &\simeq \text{const}\times\frac{T_l(E;0)v_{gl}(E)}{n_l^2(E)}G(E,t)\exp\left[-\left[B-\frac{\alpha C}{\beta-B}\right]t\right]\\
&\equiv \text{const}\times F(E,t)\exp\left[-\left[B-\frac{\alpha C}{\beta-B}\right]t\right]\\
&\simeq F_0(E,t)e^{k_1t}\exp\left[-\left[B-\frac{\alpha C}{\beta-B}\right]t\right]\simeq F_0(E-\eta(t))e^{k_1t}\exp\left[-\left[B-\frac{\alpha C}{\beta-B}\right]t\right] .
\end{aligned}
\tag{61}
$$

When $B(E)-\alpha(E)C(E)/[\beta(E)-B(E)]$ in Eq. (61) changes slowly in the region of interest, which conforms to our case, the line shape at each instant is determined by the function $F(E,t)$. Figure 5 indicates that the function $F(E,t)$ is an increasing function of time. Therefore, in Eq. (61) we have used the factorized form for $F(E,t)$ in which the function $F_0(E,t)$ is assumed to represent the normalized line shape at each instant. The choice of the exponential form, $\exp(k_1t)$, for the growth of the function $F(E,t)$ is for comparison with lifetime measurements. However, since $F_0(E,t)[F(E,t)]$ is a shifting function [Fig. 6(b)] with its peak energy defined by curve 2 in Fig. 6(a), its time dependence at fixed energies is represented by two different aspects (Fig. 7). At energies [for example curves (4) and (5) in Fig. 7] higher than E_c, which is the peak intensity energy of the function $F_0(E,t)$ at long time (about 30 ns), $F_0(E,t)$ increases to the maximum [which occurs when the peak intensity energy, $\eta(t)$, coincides with that energy E, if the fourth equality in Eq. (61) is exact] followed by a decrease to its long-time value F_0 $(E,t=30 \text{ ns})$. For $E<E_c$ [for example curve (1) in Fig. 7], $F_0(E,t)$ gradually increases to $F_0(E,t=30 \text{ nsec})$, because in this case the peak intensity energy never coincides with that energy, E. Note that $G(E,t)$ behaves in the same manner as $F_0(E,t)$ with E_c replaced by E_f which is the peak energy of the polariton distribution at long time.

From the above argument it is obvious that the time evolution of the polariton luminescence described by these equations shows a very rapid increase followed by a rapid decrease at high energy and a slow growth followed by a slow decay at low energy. Fig. 8 shows such a behavior. [Fig. 8(a) was plotted using Eq. (60).] Figure 8(b) shows the experimental data [from a large (≈ 1 mm in size) and shiny bright golden colored crystal], which show narrower widths than in Fig. 8(a). This quantitative deviation is due to the slow increase of the function $F(E,t)$ in our theory. A different combination of parameters may reduce this deviation.

In the work of Ref. 5, the experimental time-decay data were fitted in terms of a double exponential decay. In the present case, we can also approximate our theoretical solution in terms of a double exponential decay. This can be achieved by writing

$$F_0(E,t)\simeq F_0(E,\, t=30 \text{ ns})+\delta(E)e^{-\sigma(E)t} . \tag{62}$$

An examination of Fig. 7 shows that the approximation of Eq. (62) is a reasonable one. We see that for $E<E_c$, $\delta(E)<0$ and for energies much higher than E_c (for example, $E=1.874$, 1.89 eV in Fig. 7), $\delta(E)>0$ if we use Eq. (62) for the range of time after $F_0(E,t)$ has attained its maximum value. However, for the range of energies that are higher than E_c but close to E_c, it is better to approximate $F_0(E,t)$ with positive $\delta(E)$ (for example, $E=1.842$ eV in Fig. 7.) If Eq. (62) were an identity, we obviously would have $\delta(E)=-F_0(E,\, t=30 \text{ ns})$ for $E<E_c$, since $G(E,t)$ approaches zero as time goes to zero for the energy range of interest. Therefore, we have a rough estimate of

$$\delta(E)\propto -F_0(E,\, t=30 \text{ ns}) . \tag{63}$$

Now we identify $1/\{[\beta-\alpha C/(\beta-B)]-k_1\}$ as the long lifetime, $F_0(E,\, t=30 \text{ ns})$ as the preexponential factor of the long lifetime, $1/[B-\alpha C/(\beta-B)-k_1+\sigma]$ as the short lifetime and $\delta(E)$ as the preexponential factor of the short lifetime. Consequently, this provides a natural explanation for the experimental data in Ref. 5, which implies the coincidence of the three peak positions of the preexponential factors and the long-time line shape: all these peaks occur around 1.835 eV, which corresponds to E_c in the present case.

Equation (60) was fitted with a double exponential form to obtain Fig. 9, with the long lifetime $1/\{[B-\alpha C/(\beta-B)]-k_1\}$ fixed at 5.26 ns (with $k_1=1\times 10^7/\text{s}$). The decrease of short lifetime at high energy in Fig. 9(a) is associated with the fact that at higher energy the rate of peak energy decrease is larger. The latter is due to the larger density of states and the wave vector of the LPB at higher energy. [See Eqs. (30) and (41).] Therefore at higher energy the function $F_0(E,t)$ ascends quickly and also descends quickly so that it is represented by a smaller short lifetime. Figure 9(b) shows the theoretical and experimental ratios of the short lifetime preexponential factor to the long one. Again their quantitative deviation is due to the slow increase of the function $F(E,t)$ in our theory. Nevertheless, the qualitative comparison shows good agreement: both ratios are negative at low energy and positive at higher energy.

In short, the continuous red shift of the polariton distribution arising from the scattering of the acoustic phonons results in the red shift of the observed luminescence. This is also represented as the fast decay at high energy and the slow decay at low energy.

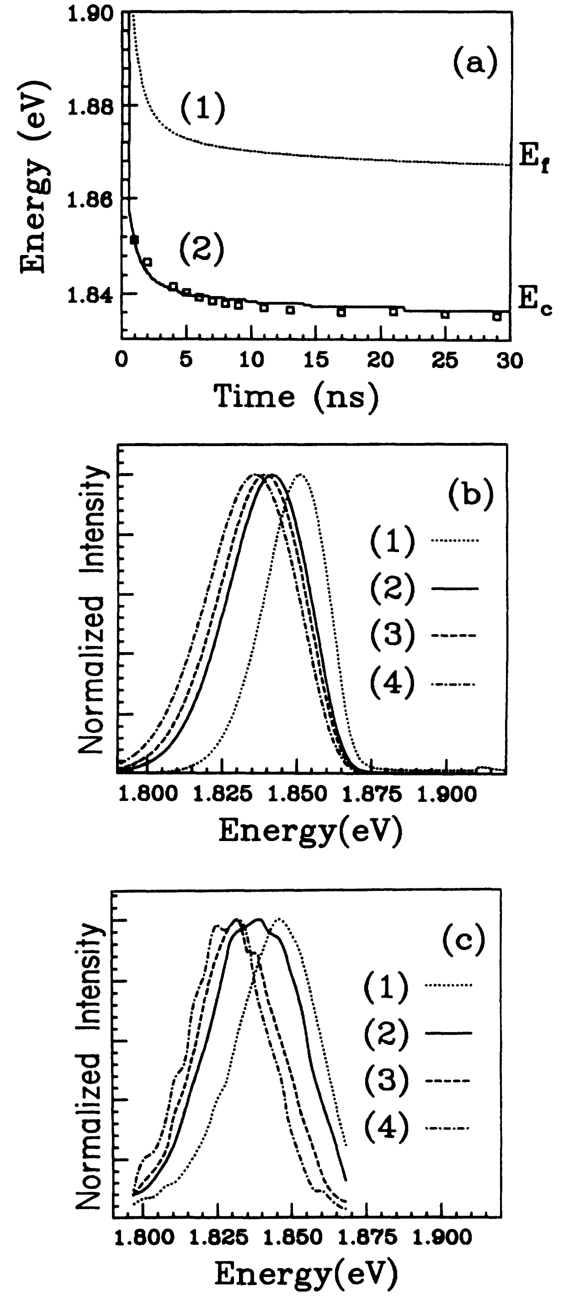

FIG. 6. (a) The (theoretical) time evolution of the maximum intensity energy, (1) $\xi(t)$ of the function $G(E,t)$ and (2) $\eta(t)$ of the luminescence line shape with the parameters in Table I. The squares are the experimental peak-energy positions of the line shapes taken from Ref. 5. (b) The theoretical and (c) experimental time-resolved line shapes (1) $I(E, t=1$ ns), (2) $I(E, t=3$ ns), (3) $I(E, t=6$ ns), and (4) $I(E, t=30$ ns).

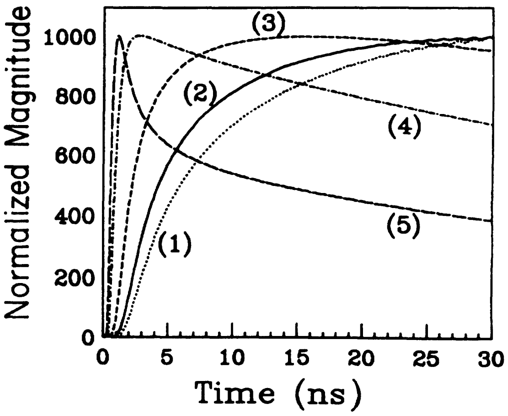

FIG. 7. Time dependence of the function $F_0(E,t)=G(E,t)(T_l v_{gl}/n_l^2)\exp(-k_1 t)$ with $k_1=1\times10^7$/s at (1) $E=1.798$ eV, (2) $E=1.814$ eV, (3) $E=1.842$ eV, (4) $E=1.874$ eV, and (5) $E=1.89$ eV.

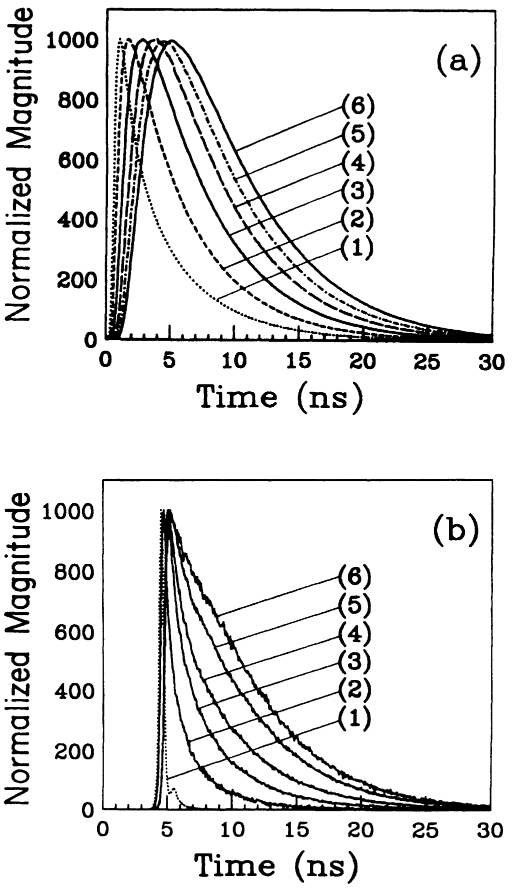

FIG. 8. (a) Theoretical time decay of luminescence intensity the $I(E,t)$ at (1) $E=1.89$ eV, (2) $E=1.874$ eV, (3) $E=1.854$ eV, (4) $E=1.834$ eV, (5) $E=1.818$ eV, and (6) $E=1.802$ eV with the parameters in Table I. (b) Experimental counterparts: (1) IRF, (2) $E=1.868$ eV, (3) $E=1.850$ eV, (4) $E=1.841$ eV, (5) $E=1.832$ eV, and (6) $E=1.814$ eV.

We now consider the size dependence of the line shape. When the crystal size decreases (S_c/V_c increases) $B(E)$ increases for energies smaller than E_L due to the increased radiative loss. However, for the energy range slightly below and above E_L, $B(E)$ is quite insensitive to the change of the crystal size because of the extremely small transmission coefficient of the LPB polaritons and the interbranch conversion coefficient to the UPB in addition to the extremely large index of refraction of the LPB. Instead, the value of $B(E)$ for that energy range is mainly determined by crystal-size independent factors, which are the interbranch scattering rate due to phonons plus the nonradiative decay rate [see Eq. (31)]. Figure 10 plots the energy dependence of $1/[B-\alpha C/(\beta-B)-k_1]$ for the three cases: (1) $S_c/V_c=0.5$/cm and $R_{\alpha 0}=2\times 10^8$/s, (2) $S_c/V_c=50$/cm and $R_{\alpha 0}=2\times 10^8$/s, and (3) $S_c/V_c=0.5$/cm and $R_{\alpha 0}=2\times 10^9$/s. Hence, in the case of a small crystal (e.g., large value of the ratio S_c/V_c) this nonuniform change of decay rate leads to the reduction of the luminescence intensity at long wavelengths [Eq. (61)], which is in agreement with the experimental data shown in Fig. 3(a). Note the three corresponding theoretical plots in Fig. 3(b) that use Eq. (60) with the parameters used for plotting Fig. 10. They show results that are consistent with experiment.

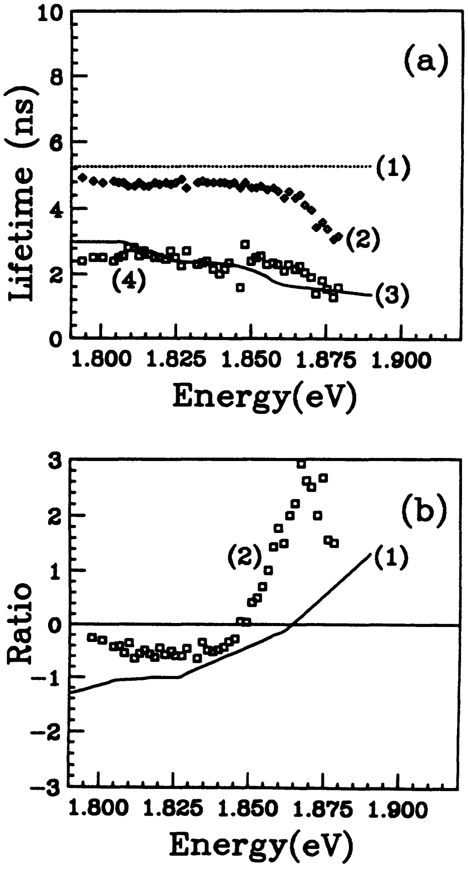

FIG. 9. (a) Lifetimes of the decay curves when the function $I(E,t)$ was fitted with a double-exponential decay. The value of the theoretical long lifetime was fixed at 5.26 ns: (1) theoretical and (2) experimental long lifetime, (3) theoretical and (4) experimental short lifetime. (b) The ratio of the short-lifetime pre-exponential factor to the long one. The theoretical curve (1) was obtained from the $I(E,t)$ and the experimental curve (2) was reconstructed from the data in Ref. 5. Both are negative at low energy and positive at high energy.

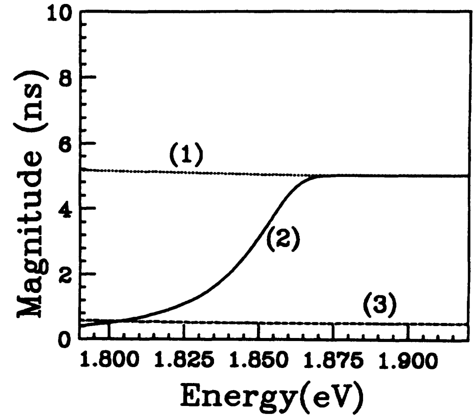

FIG. 10. The function $1/[B-\alpha c/(\beta-B)-k_1]$ for three cases: (1) $S_c/V_c=0.5$/cm and $R_{\alpha 0}=2\times 10^8$/s, (2) $S_c/V_c=50$/cm and $R_{\alpha 0}=2\times 10^8$/s, and (3) $S_c/V_c=0.5$/cm and $R_{\alpha 0}=2\times 10^9$/s.

Also it was found experimentally that the line-shape shift of a powdered crystal (≈ 20 μm in size) is different from that of a large crystal (≈ 1 mm in size): the long-time line shape shifts by only a small amount compared to the large crystal (≈ 1 mm in size). In the case of a small crystal ($S_c/V_c=50$/cm), our theoretical analysis showed smaller red shifts than the case of a large crystal ($S_c/V_c=0.5$/cm) at early time and some blue shifts at long time, although the function $G(E,t)$ does not depend on crystal size. This indicates again that our parameter combination in Table I is not a perfect choice. Additional independent experiments (see, for example, Ref. 14 for the discussion of various experimental methods) are required to improve the parameter values.

Note that we have used a smaller value of S_c/V_c (or larger crystal) in plotting our calculation in Fig. 3(b) than its actual value estimated by the physical size of the crystal. This is because we have assumed a uniform distribution of the polaritons: in reality the magnitude of polariton distribution decreases as the polariton moves from the position at which it was generated (inset of Fig. 2), which means a smaller radiative loss than in the case of a uniform distribution.

We do not have a theoretical explanation for the narrow high-energy peak that looks stationary in Fig. 4. The early-time line shape that is obtained with Eq. (60) is not narrow enough to compare with the experimental one nor is it stationary. It is, however, possible that the narrow and stationary component can be regarded as stemming from the localized exciton energy level that was formed by crystal-lattice defects or impurities. At a defect site, the trapped polaritons will be converted into a localized exciton and radiate subsequently.[16]

VIII. CONCLUDING REMARKS

Our results show that the exciton-polariton mechanism is consistent with a variety of experimental observations.

It provides a very plausible explanation for the size dependence of the luminescence line shape in the sense that the polariton dynamics are affected by the geometry of the crystal. Also our experimental data shown in Fig. 2 relating to the migration of the excited state are a natural consequence of the polariton mechanism because the polaritons have high group velocity. The scattering of polaritons with phonons alters the polariton population distribution and manifests itself as a constantly redshifting line shape (Fig. 6), which is directly responsible for the different time-evolution behavior at different energies (Fig. 8). We have shown that all of these effects are well described by the exciton-polariton dynamics, although there are some quantitative deviations. It was also shown that the time and wavelength dependence of the luminescence decay can be described by a double-exponential process as found in the work of Ref. 5. In summary, the formalism based on polariton transport explains the spatial transport of the optically excited state, the crystal size and quality dependence of the line shape, the time evolution of the line shape, the fast decay at high and slow decay at low energies, and the observed double-exponential decay.

ACKNOWLEDGMENTS

We are grateful to R.-H. Huang and M. G. DeBacker for providing the samples. Many illuminating discussions with M. Holtz are also greatly appreciated. This work was supported by the U.S. National Science Foundation Division of the Materials Research Grant No. DMR 87-17763 and by the Michigan State University Center for Fundamental Materials Research.

---

[1] Cryptand[2.2.2] is a bicyclic polyether that encapsulates the Na^+ ion. It has the molecular formula $N(CH_2CH_2OCH_2CH_2OCH_2CH_2)_3N$.

[2] J. L. Dye, Prog. Inorg. Chem. **32**, 327 (1984); J. L. Dye and M. G. DeBacker, Ann. Rev. Phys. Chem. **38**, 271 (1987).

[3] F. J. Tehan, B. L. Barnett, and J. L. Dye, J. Am. Chem. Soc. **96**, 7203 (1974).

[4] J. L. Dye, R. H. Huang, and D. L. Ward, J. Coord. Chem. B **18**, 121 (1988).

[5] R. S. Bannwart, S. A. Solin, M. G. DeBacker, and J. L. Dye, J. Am. Chem. Soc. **111**(15), 5552 (1989).

[6] Recent measurements showed that the same machine used in the work of Ref. 5 had a temperature difference between the cold finger and the sample site: when the cold finger was at 11 K, the sample site was at 22 K. Therefore we have used a temperature of 20 K in constructing the theoretical curves.

[7] J. Papaioannou, S. Jaenicke, and J. L. Dye, J. Solid State Chem. **67**, 122 (1987).

[8] M. G. DeBacker, A. Sieradzan, G. Xu, Ta-Ryeong Park, and J. L. Dye (unpublished results).

[9] D.-H. Shin, A. S. Ellaboudy, J. L. Dye, and M. G. DeBacker (unpublished results).

[10] J. L. Dye, M. R. Yemen, M. G. DaGue, and J.-M. Lehn, J. Chem. Phys. **68**, 1665 (1975).

[11] D. V. O'Connor and D. Phillips, *Time-Correlated Single Photon Counting* (Academic, London, 1984).

[12] J. J. Hopfield, Phys. Rev. **112**, 1555 (1958).

[13] S. I. Pekar, Zh. Eksp. Teor. Fiz. **33**, 1022 (1958) [Sov. Phys. JETP **6**, 785 (1958)].

[14] F. Bassani and L. C. Andreani, in *Excited-State Spectroscopy in Solids*, edited by U. M. Grassano and N. Terzi (North-Holland, Amsterdam, 1987), p. 1.

[15] Y. Toyozawa, Suppl. Prog. Theor. Phys. **12**, 111 (1959).

[16] H. Sumi, J. Phys. Soc. Jpn. **41**, 526 (1976).

[17] F. Askary and P. Y. Yu, Phys. Rev. B **31**, 6643 (1985).

[18] D. E. Cooper and P. R. Newman, Phys. Rev. B **39**, 7341 (1988).

[19] V. V. Travnikov and V. V. Krivolapchuk, Zh. Eksp. Teor. Fiz. **85**, 2087 (1983) [Sov. Phys. JETP **58**, 1210 (1983)].

[20] T. Steiner, M. L. W. Thewalt, E. S. Koteles, and J. P. Salerno, Phys. Rev. B **34**, 1006 (1986).

[21] A. Bonnot and C. Benoît à la Guillaume, in *Polaritons*, edited by E. Burstein and F. De Martini (Pergamon, New York, 1975), p. 197.

[22] V. V. Rossin, Fiz. Tverd. Tela (Leningrad) **32**, 801 (1990) [Sov. Phys. Solid State **32**, 472 (1989)].

[23] The actual structure of sodium cryptand[2.2.2] sodide is anisotropic. See Ref. 3.

[24] J. J. Hopfield and D. G. Thomas, Phys. Rev. **132**, 563 (1963).

[25] W. C. Tait and R. L. Weiher, Phys. Rev. **178**, 1404 (1969).

[26] D. A. McQuarrie, *Statistical Mechanics* (Harper & Row, New York, 1976).

[27] R. H. Good, Jr. and T. J. Nelson, *Classical Theory of Electric and Magnetic Fields* (Academic, New York, 1971), p. 351.

[28] A. Selkin, Phys. Status Solidi B **83**, 47 (1977).

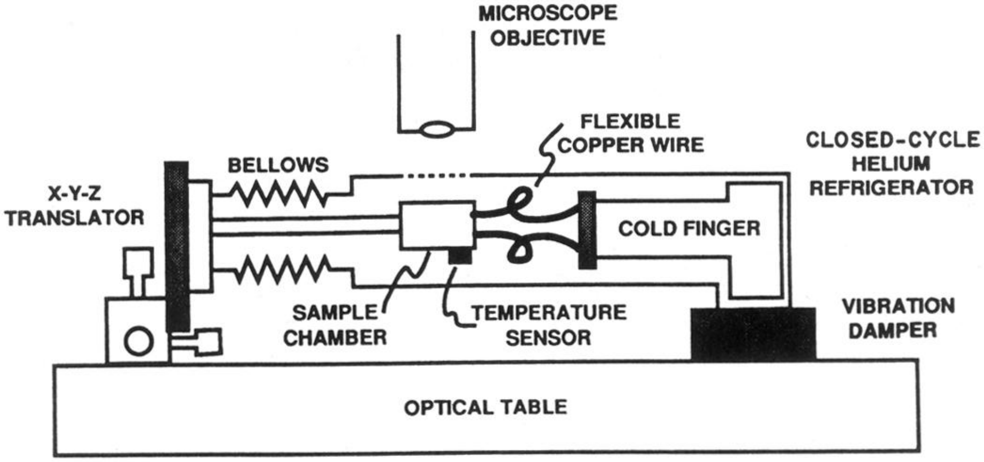

FIG. 1. Diagram of the low-temperature vibration isolated sample chamber with microscope.